RESEARCH   **Open Access**

The Lattice Distortion-Induced Ferromagnetism in the Chemical-Bonded MoSe$_2$/WSe$_2$ at Room Temperature

Shiu-Ming Huang[*], Pin-Cing Wang and Pin-Cyuan Chen

Abstract

Ferromagnetism to non-ferromagnetism transition is detected in a chemically bonded MoSe$_2$/WSe$_2$ powder with different thermal annealing temperatures. All samples exhibit ferromagnetism and Raman redshift, except for the 1100 °C thermally annealed sample in which the MoSe$_2$ and WSe$_2$ are thermally dissociated and geometrically separated. The element analysis reveals no significant element ratio difference and detectable magnetic elements in all samples. These results support that, in contrast to the widely reported structure defect or transition element dopant, the observed ferromagnetism originates from the structure distortion due to the chemical bonding at the interface between MoSe$_2$ and WSe$_2$.

Keywords: Ferromagnetism, Chemically bonded, Lattice distortion, Two-dimensional transition-metal dichalcogenides

Introduction

Spintronics is an approach to manipulating spin polarization and to realizing spin-based functionalities. Dilute magnetic semiconductor (DMS) is one of the promising materials for spintronics applications [1, 2]. The original idea is doping magnetic elements into a semiconductor host, and thus, the material possesses both semiconductor and magnetic behaviors. The DMS has been widely studied in group III-V and II-VI semiconductor-based systems and reveals intrinsic ferromagnetism. However, low Curie temperatures and the intrinsic/extrinsic mechanism disputation limit its application potential [1, 2]. It has been shown that the spin-momentum locking effect is able to induce a non-equilibrium spin accumulation in topological insulators, and this spin accumulation in the topological surface states can be electrically manipulation [3, 4].

The quantum anomalous Hall effect is the quantum Hall effect without an external magnetic field, but instead due to intrinsic ferromagnetism [5]. The quantum anomalous Hall effect is expected to play a role in spintronics. It has been theoretically [5–8] and experimentally demonstrated on the extrinsic ferromagnetic elements in the topological insulator [9–12]. On the hand, it is theoretically and experimentally reported that the structure manipulation could lead to intrinsic ferromagnetism in two-dimensional transition-metal dichalcogenides (2D TMDs) [13–16]. As well as the extrinsic ferromagnetic elements doped, the intrinsic structure manipulation or distortion might lead to ferromagnetism in 2D TMDs. The recent investigation shows that zigzag structure or lattice defect might lead to intrinsic ferromagnetism in 2D TMDs at room temperature [17–27]. Experimental work exhibits that coercivity field, remanence, and saturated magnetization are sensitive to host materials and structure configurations, and it reveals a wide range of performance efficiency. To maximize ferromagnetism, lots of artificial treatments were performed. Most studies mainly focus on the combination of various magnetic

*Correspondence: smhuang@mail.nsysu.edu.tw

Department of Physics, National Sun Yat-Sen University, 80424 Kaohsiung, Taiwan

Huang *et al. Nanoscale Research Letters*   (2022) 17:55

Page 2 of 7

elements and host 2D TMDs, as well as the structure and defect treatment methods [17–22]. A recent work exhibits two magnetic elements co-doping treatment in MoS_2 and WSe_2 single crystals, and the pinning effect leads to great enhancement of magnetization and coercivity field [28–32]. The ion implantation induces a large number of defects and lattice strains, which serve as pinning centers. The two magnetic elements lead to directional anisotropy coupling strength, and the ferromagnetism is enhanced through the anisotropy distortion. Following this concept, it is interesting to investigate how ferromagnetism would be in a chemical-bonded 2D TMDs.

The chemical-bonded $MoSe_2$/WSe_2 powder (MWS powder) with different thermal annealing temperatures is studied. Ferromagnetism to non-ferromagnetism transition is detected in a chemical-bonded MWS powder with different thermal annealing temperatures. Additionally, a redshift in the Raman peak appears only in systems with "clay-bond" $MoSe_2$ and WSe_2, but not in systems without a geometric connection between $MoSe_2$ and WSe_2. The magnetic field-dependent magnetism shows that a hysteresis loop is observed in systems with chemical bonding at the boundary between $MoSe_2$ and WSe_2, and no hysteresis loops in the system without chemical bonding between $MoSe_2$ and WSe_2. These results support that in contrast to the widely reported structure defect or transition element dopant, the ferromagnetism originates from the structure distortion due to the chemical bonding at the interface between $MoSe_2$ and WSe_2.

Experimental Method

The chemical-bonded $MoSe_2$/WSe_2 powder (MWS powder) is a commercial product and was purchased from SixCarbon Technology Co. The purchased MWS powder was vacuum-sealed in a glass tube with a pressure of 10^{-3} torr and then, thermally annealed. The MWS powder was heated up to the target temperatures at a rate of 2.7 °C/min, and stayed at the target temperature for 1 hour. After the thermal annealing, it was naturally cooled down to room temperature.

The X-ray diffraction (XRD) was performed in a D2 phaser using the Cu Kα radiation with a scan step of 0.1°. Raman spectroscopy was performed in the HORIBA, HR 800 with wavelength 633 nm and scan step of 0.3 cm^{-1}. The model of X-ray Photoelectron Spectroscope (XPS) is ULVAC-PHI, PHI 5000 Versa Probe, and the Scanning ESCA Microprobe was used to detect the sample phase composition. The XPS spectra were acquired using a monochromat Al Kα source whose energy is about 1486.7 eV. An analyzer acceptance angle of $\pm 8°$ and take-off angle of 45°, and the pass energy of 15 eV was used for this study. The binding energy scale is calibrated using the ASTM procedure.

The JEOL-6330 Field-Emission SEM backscattering electron image (BEI) mode was used to verify the atomics ratio. Under the BEI mode, one distinguished the $MoSe_2$ and WSe_2 easily by analyzing the secondary electron. The electron beam actually penetrates the sample at about a micrometer depth and scatters back as secondary electrons. The efficiency of backscattering would increase as the atomic number increased. As the result, under BEI mode, the lighter part represents the location of the heavier atom. To remove the possibility of the existence of other atoms, the mapping mode was used. In this mode, SEM can roughly scan a big area (as big as the holder of SEM) on the sample and show the possible existence of atoms in the sample. To exclude the possible impurities and take a higher accuracy atom ratio in our sample, the point mode was used on different shaded areas. Also, in order to get the accurate ratio statistics of the molecular number of $MoSe_2$ and WSe_2, the point mode was applied over hundreds of points. The result implied that the ratio of $MoSe_2$ and WSe_2 is roughly 1.

Magnetism measurements were performed using the standard technique in a SQUID MPMS-3 magnetometer (Quantum Design), and the magnetic field step is 50 Oe.

Results and Discussion

Figure 1 shows the XRD spectrum of the MWS powder with different thermal annealing temperatures. It reveals sharp peaks and the XRD peak intensity over background noise reaching 440 for (002) peaks in all thermal annealing temperatures. Both $MoSe_2$ and WSe_2 are hexagonal structures, and the XRD peak is consistent with the database of hexagonal structures. No peak intensity and
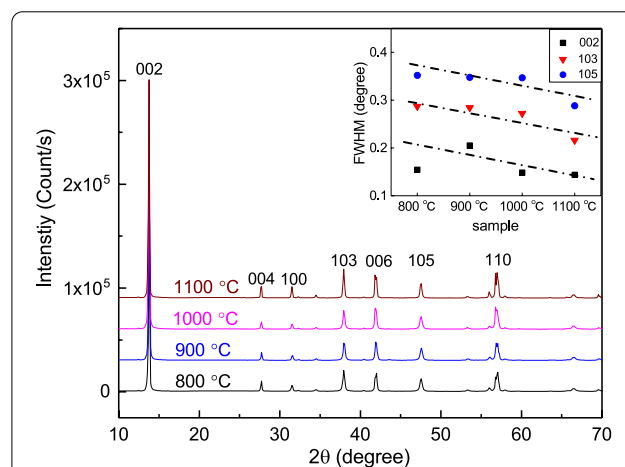

Fig. 1 The XRD spectrum of the $MoSe_2$/WSe_2 powder at different thermal annealing temperatures. No obvious peak shift was observed. The inset reveals that the full-width at half height of XRD peaks slightly decrease at higher annealing temperatures

Huang *et al. Nanoscale Research Letters*   (2022) 17:55

Page 3 of 7

obvious peaks shift were observed in all thermal annealing temperatures, and that indicates that the thermal annealing does not change the crystal structure. Figure 1 inset reveals the full-width at half height (FWHH) of XRD peaks is roughly $0.2 \sim 0.4$. The FWHH slightly decreases as the annealing temperature increases. This supports that the thermal annealing further slightly decreases lattice defects and crystallizes MWS powders.

Figure 2a–f shows the SEM image of MWS in the backscattering emission image (BEI) mode. They are thermally annealed in temperatures from 800 to 1100 °C. Figure 2a–c shows that the $MoSe_2$ and WSe_2 are "claybond." Figure 2d–f shows that the $MoSe_2$ and WSe_2 had

thermally dissociated and have rare geometric connection after 1100 °C thermal annealing. The $MoSe_2$ and WSe_2 melting points are roughly 1200 °C which is very close to the highest thermal annealing temperature 1100 °C in this work. That might be the reason why the $MoSe_2$ and WSe_2 are completely dissociated after 1100 °C thermal annealing. The EDS result supports that the W:Se = 1:2 in the light zone and Mo:Se = 1:2 in the dark zone. Electron probe micro-analyzer (EPMA) was used to determine the material composition ratio. The EPMA supports that the W:Se = 1:2 in the light zone, Mo:Se = 1:2 in the dark zone, and $MoSe_2$:$WSe_2 \approx 1:1$. The thermal energy assists the atom in crossing the
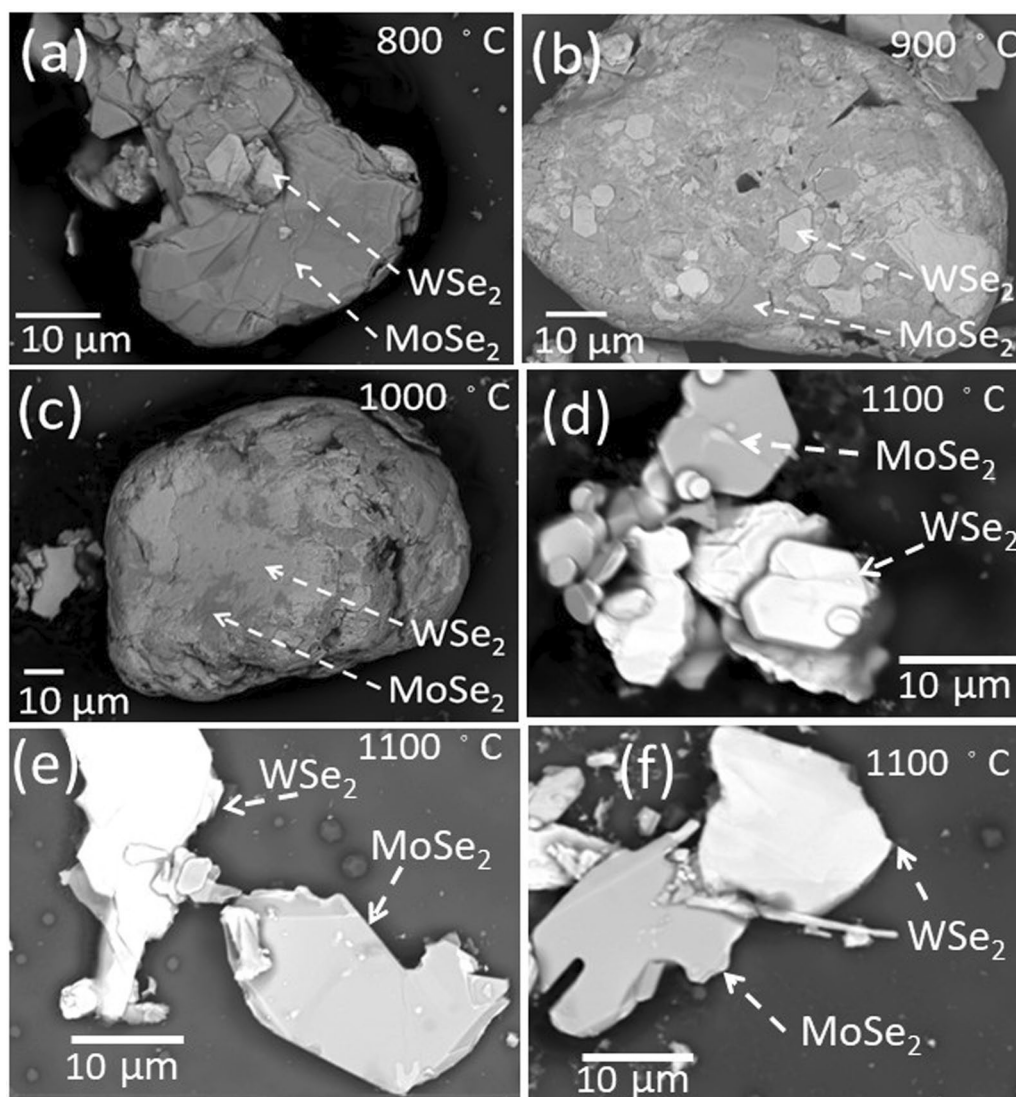

Fig. 2 (**a**)–(**f**) show the SEM image of the $MoSe_2$/WSe_2 powder with different thermal annealing temperatures in the backscattering emission image mode. The EPMA result supports that the W:Se = 1:2 in the light zone and Mo:Se = 1:2 in the dark zone. The $MoSe_2$ and WSe_2 individually locate after 1100° thermal annealed. The others are chemically bonded

potential barrier. Atoms prefer to move to the position with lower energy and bond together, and that makes the defect gather together. At higher temperatures, the defects gather together form a bigger defect. As shown in Fig. 2a–c, the morphology exhibits more and bigger "hole" at higher thermal annealing temperatures. These cracks completely separate the $MoSe_2$ and WSe_2 at a critical temperature above 1000 °C. It is reported that thermal annealing induces S vacancies in WS_2 and MoS_2. The XPS reveals no obvious Mo, W and Se vacancy difference in the different thermally annealed MWS. Structure vacancy might shift the peak position and suppress the peak intensity. The peak shift and the peak intensity suppression are not observed in Fig. 1, since the thermal annealing-induced element vacancy or structural defect is not an important factor in our MWS.

Figure 3a–d shows the M-H loop at room temperature, and it exhibits a hysteresis loop in the MWS with 800 °C (MWS-800), 900 °C (MWS-900), and 1000 °C (MWS-1000). It is a ferromagnetism feature. The M-H loop reveals a negative linear diamagnetism in the MWS 1100 °C (MWS-1100). The M-H loop is completely overlapping at a wide range of magnetic fields, and no detectable hysteresis loops are observed in the MWS-1100. To further confirm the existence of the observed ferromagnetism, the field cool (FC) and the zero-field cool (ZFC)

processes are performed. As shown in the inset of Fig. 3, the FC and ZFC magnetization splits in the MWS-800, MWS-900, and MWS-1000, and it completely overlapped in the MWS-1100 (Fig. 4). This implies that the ferromagnetism in the MWS-800, MWS-900, and MWS-1000 and is consistent with the M-H loop in Fig. 3.

Moreover, we seek to know the source of the ferromagnetism and the reason why ferromagnetism is not detected in the MWS-1100. It is known that a slight magnetic or transition element dopant might lead to great ferromagnetism in 2D TMDs.

The MWS with different thermal annealing temperatures are from the same raw material and have no difference in treatment processes and equipment. It is expected that the magnetic element concentration would be the same and its contribution to the ferromagnetism would be similar. Figure 3 exhibits that the coercivity field, remanence, and M-H curves are completely different. The MWS-1100 even shows no hysteresis loops. The coercivity fields and magnetization in the MWS-1000 are one-order larger than those in the MWS-800 and MWS-900. On the other hand, the extracted saturated magnetization in our MWS-800 is roughly 0.0004 emu/g (Table 1). This corresponds to 0.4% of magnetic elements (such as Fe, Co, or Ni) contributed to magnetization. This large concentration is within the detectable range in the
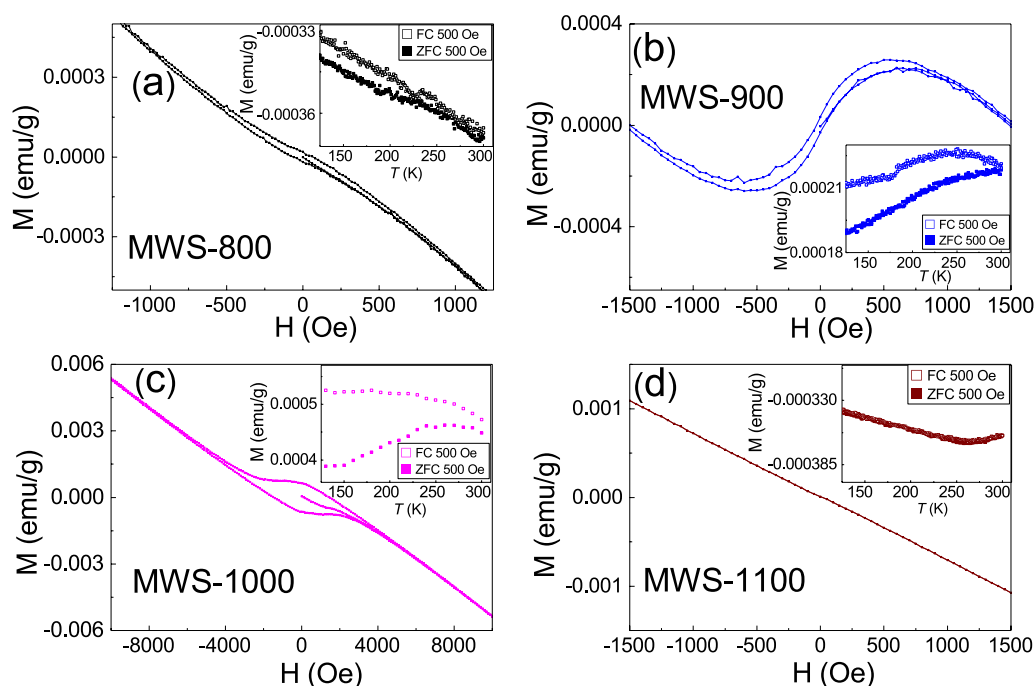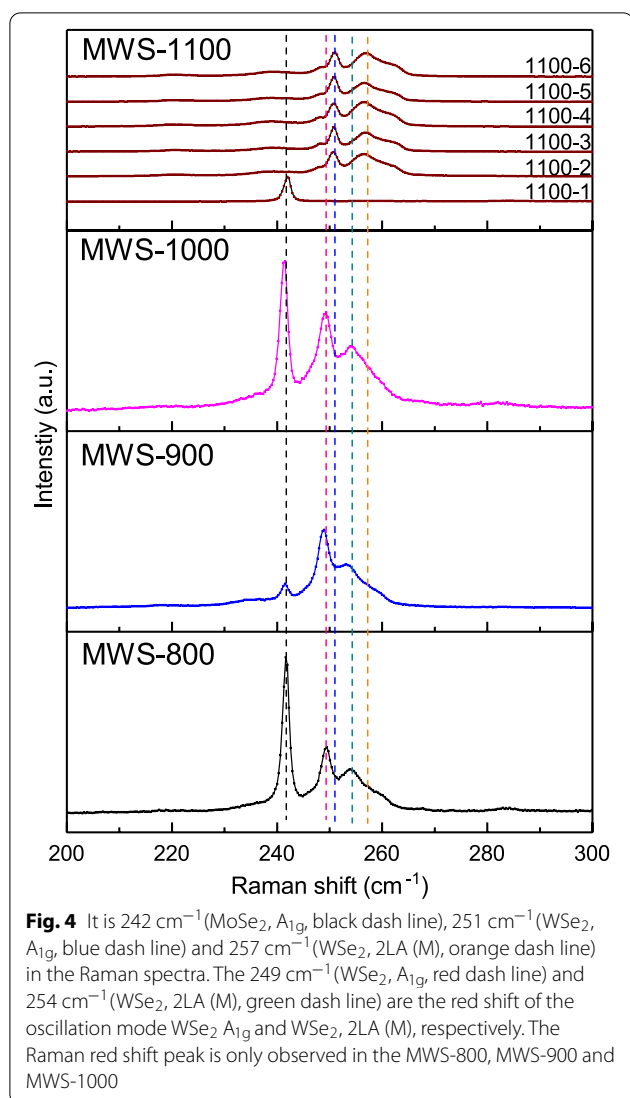

Fig. 3 The magnetic field-dependent magnetization. Figure (**a**–**c**) reveals hysteresis loops. Figure **d** shows diamagnetism feature and no hysteresis loops. The inset shows the magnetization of field cool and zero field cool processes. The field cool and zero field cool curve split in all of the samples except for the MWS-1100

Huang *et al. Nanoscale Research Letters*   (2022) 17:55

Page 5 of 7

Fig. 4 It is 242 cm^{-1} (MoSe$_2$, A$_{1g}$, black dash line), 251 cm^{-1} (WSe$_2$, A$_{1g}$, blue dash line) and 257 cm^{-1} (WSe$_2$, 2LA (M), orange dash line) in the Raman spectra. The 249 cm^{-1} (WSe$_2$, A$_{1g}$, red dash line) and 254 cm^{-1} (WSe$_2$, 2LA (M), green dash line) are the red shift of the oscillation mode WSe$_2$ A$_{1g}$ and WSe$_2$, 2LA (M), respectively. The Raman red shift peak is only observed in the MWS-800, MWS-900 and MWS-1000

EPMA, but our experiment reveals no detectable magnetic elements in all MWS. Our EDS analysis also supports that no un-avoided magnetic or transition elements in the MWS.

The ferromagnetism might originate from the lattice defect or zigzag structure [32–42]. Figure 1 shows that the XRD peaks are extremely sharp and the XRD peak signal to background noise ratio and FWHM are almost the same in different MWSs. The structure defect should not lead to the big difference in the observed ferromagnetism features. However, there is ferromagnetism to non-ferromagnetism transition. Moreover, the defect and zigzag should be uniformly distributed in all MoSe$_2$ and WSe$_2$ blocks in the MWS. The coercivity field is sensitive to host materials and amount of defect. It is reported that the vacancy-induced ferromagnetism coercivity field in WSe$_2$ is roughly one order higher than that in MoSe$_2$. In the case where the vacancy and defect dominate the observed ferromagnetism in our MWS, one would expect to observe two hysteresis loop steps from individual MoSe$_2$ and WSe$_2$ contributions. Figure 3a–c shows only one hysteresis loop in all MWSs. On the contrary, it is not reasonable that the defect is completely from specific materials (MoSe$_2$ or WSe$_2$), so one cannot simply ascribe the observed one-step hysteresis loop to the contribution from specific materials.

The ferromagnetism is studied in the MoS$_{2-x}$Se$_x$ crystal, and results reveal that the ferromagnetism is sensitive to the Se/S ratio. It exhibits the largest ferromagnetism in the Mo(S$_{0.49}$Se$_{0.51}$)$_2$ nanosheet [43]. This supports that similar to the element vacancy or the zigzag edge structure, the element replacement and dislocation might also lead to the ferromagnetism. Furthermore, ferromagnetism and magnetoresistance hysteresis is observed in a molecular-beam epitaxy grown non-magnetic group IV Ge$_{1-x}$Sn$_x$ thin film on Ge buffer layer with a high-resistivity Si(001) as substrate. It forms a Ge$_{1-x}$Sn$_x$ alloys at the interface between Ge and Ge$_{1-x}$Sn$_x$ thin films. The observed ferromagnetism is understood as the inversion symmetry breaking from atomic disordering in the alloy at the interface between Ge and Ge$_{1-x}$Sn$_x$ [47]. These experimental results support that the element dislocation might lead to the ferromagnetism, in addition to the structure defect, transition element dopant, or magnetic dopant.

As shown in Fig. 2, the BEI reveals that the MoSe$_2$ and WSe$_2$ zones are smoothly bonding and might lead to the Mo$_x$W$_{1-x}$Se$_2$ structure. This chemical bonding at the MoSe$_2$ and WSe$_2$ interface would lead to slight lattice bonding distortion and that leads to the ferromagnetism. The observed ferromagnetic hysteresis loop might originate from this effect. Theoretical calculation demonstrates that the structure defect would induce

Table 1 List of Raman spectra peak in bulk MoSe$_2$ and WSe$_2$

Material mode	MoSe$_2$ A$_{1g}$	MWS red shift	WSe$_2$ A$_{1g}$	MWS red shift	WSe$_2$ 2LA(M)
unit	cm^{-1}	cm^{-1}	cm^{-1}	cm^{-1}	cm^{-1}
800	241.6	249.4	X	254.3	X
900	241.5	249.0	X	253.8	X
1000	241.5	249.3	X	254.8	X
1100-1	241.9	X	X	X	X
1100-2	X	X	250.7	X	256.6
1100-3	X	X	250.7	X	256.9
1100-4	X	X	250.7	X	256.3
1100-5	X	X	250.7	X	256.6
1100-6	X	X	251.0	X	256.9

Huang *et al. Nanoscale Research Letters*   (2022) 17:55

Page 6 of 7

ferromagnetism in MoS_2 monolayer and mentioned the defect plays an important role in the magnetic properties [44]. Experimentally, it is demonstrated the defect would lead to ferromagnetism in various kinds of 2D TMDs [32–42]. The Raman spectrum is a sensitive tool to detect the chemical bonding configuration. To identify the chemical bonding condition between $MoSe_2$ and WSe_2, the Raman spectrum was performed in MWS powders. Figure shows the Raman spectra of MWS. There are three main oscillation modes in the spectra [45]. It is 242 cm^{-1} ($MoSe_2$, A_{1g}, black dash line), 251 cm^{-1} (WSe_2, A_{1g}, blue dash line), and 257 cm^{-1} (WSe_2, 2LA (M), orange dash line) in the MWS-1100. They are 242 cm^{-1} ($MoSe_2$, A_{1g}, black dash line), 249 cm^{-1} (WSe_2, A_{1g}, red dash line) and 254 cm^{-1} (WSe_2, 2LA (M), green dash line) in the MWS-800, MWS-900, and MWS-1000. As shown in Fig. 2, the $MoSe_2$ and WSe_2 are completely separated in the MWS-1100, and the $MoSe_2$ and WSe_2 are partially connected in the MWS-800, MWS-900, and MWS-1000. The chemical bonding would directly influence atoms' oscillation frequencies and that leads to the Raman peak shift. This implies that the 249 cm^{-1} (WSe_2, A_{1g}, red dash line) and 254 cm^{-1} (WSe_2, 2LA (M), green dash line) originate from the red shift of the oscillation mode WSe_2 A_{1g} and WSe_2, 2LA (M). The red shift in the Raman peak is only observed in the MWS-800, MWS-900, and MWS-1000. Table lists the observed Raman spectra. The previous work shows that a larger red shift is observed in the $Mo_xW_{1-x}Se_2$ with more Mo elements [46]. Upon further examination of the BEI image, it is believed that the Raman red shift should originate from the chemical bonding at the interface of $MoSe_2$ and WSe_2 blocks. This slight atom dislocation would break the lattice symmetry that leads to the structure distortion at the boundary between $MoSe_2$ and WSe_2. This distortion is equivalent to the structure defects, inducing ferromagnetism [47].

Conclusion

Ferromagnetism to non-ferromagnetism transition is detected in a chemical-bonded $MoSe_2$/WSe_2 powder with different thermal annealing temperatures. The $MoSe_2$/WSe_2 exhibits the ferromagnetism and Raman red shift, except for the 1100 °C thermally annealed sample in which the $MoSe_2$ and WSe_2 are thermally dissociated and geometrically separated. The element analysis reveals no significant element ratio difference and detectable magnetic elements in all samples. Our experimental studies conclude that in contrast with the widely reported structure defect or transition element dopant, the ferromagnetism originates from the structure distortion due to the chemical bonding at the interface between $MoSe_2$ and WSe_2.

References

1. Prinz GA (1998) Magnetoelectronics. Science 282:1660–1663
2. Ohno H et al (2000) Electric-field control of ferromagnetism. Nature 408:944–946
3. Li CH et al (2014) Electrical detection of charge-current-induced spin polarization due to spin-momentum locking in Bi_2Se_3. Nat Nanotechnol 9:218
4. Li P et al (2018) Spin-momentum locking and spin-orbit torques in magnetic nano-heterojunctions composed of Weyl semimetal WTe_2. Nat Commun 9:3990
5. Weng H et al (2015) Quantum anomalous Hall effect and related topological electronic states. Adv Phys 64:227
6. Checkelsky JG et al (2014) Trajectory of the anomalous Hall effect towards the quantized state in a ferromagnetic topological insulator. Nat Phys 10:731
7. Xu G et al (2015) Quantum anomalous hall effect in magnetic insulator heterostructure. Nano Lett 15:2019–2023
8. Qi S et al (2016) High-temperature quantum anomalous hall effect in *n-p* codoped topological insulators. Phys Rev Lett 117:056804
9. Liu W et al (2015) Atomic-scale magnetism of Cr-Doped Bi_2Se_3 thin film topological insulators. ACS Nano 9:10237–10243
10. Chen T et al (2015) High-mobility Sm-doped Bi_2Se_3 ferromagnetic topological insulators and robust exchange coupling. Adv. Mat. 27:4823
11. Haazen PPJ et al (2012) Ferromagnetism in thin-film Cr-doped topological insulator Bi_2Se_3. Appl Phys Lett 100:082404
12. Niu C et al (2011) Quantum anomalous Hall effect in doped ternary chalcogenide topological insulators $TlBiTe_2$ and $TlBiSe_2$. Appl Phys Lett 98:252502

Huang *et al. Nanoscale Research Letters*   (2022) 17:55

Page 7 of 7

13. Eda G et al (2012) Coherent atomic and electronic heterostructures of single-layer MoS$_2$. ACS Nano 6:7311–7317
14. Chou SS et al (2015) Understanding catalysis in a multiphasic two-dimensional transition metal dichalcogenide. Nat Commun 6:8311
15. Manchanda P et al (2015) Magnetism of Ta dichalcogenide monolayers tuned by strain and hydrogenation. Appl Phys Lett 107:032402
16. Shi H et al (2013) Strong ferromagnetism in hydrogenated monolayer MoS$_2$ tuned by strain. Phys Rev B 88:205305
17. Tao L et al (2017) Experimental and theoretical evidence for the ferromagnetic edge in WSe$_2$ nanosheets. Nanoscale 9:4898–4906
18. Matte HSSR et al (2012) Synthesis, characterization, and properties of few-layer metal dichalcogenides and their nanocomposites with noble metal particles, polyaniline, and reduced graphene oxide. ZAAC 638:2617–2624
19. Huo N et al (2014) Edge-states ferromagnetism of WS$_2$ nanosheets. Appl Phys Lett 104:202406
20. Cai L et al (2015) Vacancy-induced ferromagnetism of MoS$_2$ nanosheets. J Am Chem Soc 137:2622–2627
21. Rohini S, Sudakar C (2020) Tailoring magnetically active defect sites in MoS$_2$ nanosheets for spintronics applications. ACS Appl. Nano Mater. 3:576–587
22. Yang Z et al (2015) Realization of high Curie temperature ferromagnetism in atomically thin MoS$_2$ and WS$_2$ nanosheets with uniform and flower-like morphology. Nanoscale 7:650–658
23. Mao X et al (2013) Ferromagnetism in exfoliated tungsten disulfide nanosheets. Nanoscale Res Lett 8:430
24. Ding X et al (2019) Enhanced ferromagnetism in WS$_2$ via defect engineering. J Alloy Compd 772:740–744
25. Joseph A et al (2021) Structural, optical, magnetic and electrochemical properties of hydrothermally synthesized WS$_2$ nanoflakes. J Mater Res 36:884–895
26. Xia B et al (2015) Zigzag-edge related ferromagnetism in MoSe$_2$ nanoflakes. Phys Chem Chem Phys 17:32505–32510
27. Xing X et al (2018) Room temperature ferromagnetism and its origin for amorphous MoSe$_2$ nanoflowers. Appl Phys Lett 112:122407
28. Wang J et al (2016) Robust ferromagnetism in Mn-doped MoS$_2$ nanostructures. Appl Phys Lett 109:092401
29. Ahmed S et al (2019) High coercivity and magnetization in WSe$_2$ by Codoping Co and Nb. Small 16:1903173
30. Ahmed S et al (2020) Colossal magnetization and giant coercivity in ion-implanted (Nb and Co) MoS$_2$ Crystals. ACS Appl Mater Interfaces 12:58140–58148
31. Ahmed S et al (2017) Inducing high coercivity in MoS$_2$ nanosheets by transition element doping. Chem Mater 29:9066–9074
32. Ahmed S et al (2017) Magnetic properties of Co doped WSe$_2$ by implantation. J Alloy Compd 731:25–31
33. Mathew S et al (2012) Magnetism in MoS$_2$ induced by proton irradiation. Appl Phys Lett 101:102103
34. Ren H, Zhang L, Xiang G (2020) Web buckle-mediated room-temperature ferromagnetism in strained MoS$_2$ thin films. Appl Phys Lett 116:012401
35. Ahmed S et al (2018) Annealing effect on the ferromagnetism of MoS$_2$ nanoparticles. J Alloy Compd 746:399–404
36. Tongay S et al (2012) Magnetic properties of MoS$_2$: Existence of ferromagnetism. Appl Phys Lett 101:123105
37. Zhou Q et al (2018) Robust ferromagnetism in zigzag-edge rich MoS$_2$ pyramids. Nanoscale 10:11578–11584
38. Hu W et al (2019) Synergetic effect of substitutional dopants and sulfur vacancy in modulating the ferromagnetism of MoS$_2$ nanosheets. ACS Appl Mater Interfaces 11:31155–31161
39. Han SW et al (2016) Electron beam-formed ferromagnetic defects on MoS$_2$ surface along 1T phase transition. Sci Rep 6:38730
40. Zhang R et al (2014) Ferromagnetism in ultrathin MoS$_2$ nanosheets: from amorphous to crystalline. Nanoscale Res Lett 9:586
41. Qi R et al (2017) Towards well-defined MoS$_2$ nanoribbons on a large scale. Chem Commun 53:9757–9760
42. Habib M et al (2018) Ferromagnetism in CVT grown tungsten diselenide single crystals with nickel doping. Nanotechnology 29:115701
43. Xia B et al (2015) Hierarchical ultrathin Mo(S$_x$Se$_{1-x}$)$_2$ nanosheets with tunable ferromagnetism and efficient hydrogen evolution reaction activity: towards defect site effect. CrystEngComm 17:6240–6425
44. Wang Y et al (2017) Defects engineering induced room temperature ferromagnetism in transition metal doped MoS$_2$. Mater Designs 121:77–84
45. Terrones H et al (2014) New first order Raman-active modes in few layered transition metal dichalcogenides. Sci Rep 4:4215
46. Sun Y et al (2017) Low-temperature solution synthesis of transition metal dichalcogenide alloys with tunable optical properties. J Am Chem Soc 139:11096–11105
47. Lin B-C et al (2021) Spontaneous ferromagnetism and magnetoresistance hysteresis in Ge$_{1-x}$Sn$_x$ alloys. Science Bulletin 66:1375

Publisher's Note